Available online at www.sciencedirect.com
SCIENCE DIRECT®
Journal of Computational Physics 207 (2005) 261–281
JOURNAL OF COMPUTATIONAL PHYSICS
www.elsevier.com/locate/jcp

A new flux–vector splitting compact finite volume scheme

T.K. Sengupta [a,*], R. Jain [b], A. Dipankar [a]

[a] Department of Aerospace Engineering, IIT Kanpur, UP 208016, India
[b] Department of Mechanical Engineering, IIT Guwahati, Assam 781039, India

Received 12 July 2004; received in revised form 18 January 2005; accepted 19 January 2005
Available online 23 March 2005

Abstract

A new high resolution finite volume method is proposed here that uses flux–vector splitting as the building block to represent the physical processes. The high accuracy projection in space is obtained here, inter alia, by using some compact schemes of Sengupta et al. [1] and Lele [2] – that have extremely high accuracy in spectral plane. This produces a new class of finite volume (FV) scheme for spatial discretization, that has been analyzed for spectral accuracy, numerical stability and dispersion relation preservation (DRP) property following the full-domain analysis method of [1] using two different time integration strategies. These combination of spatial and temporal methods have been tested for two linear wave problems, reported in [1,3] and the solution of Burgers' equation is compared with the analytical results presented in Adams and Shariff [4]. The shock capturing method is based on the proposed technique in [5], that does not require the usage of any nonlinear differencing techniques or limiters.

To show that the proposed method can also handle irregular grids, the Burgers' equation is solved using non-uniform grids. Also to demonstrate the utility of the proposed scheme to solve practical problems, the benchmark problem of nonlinear wave propagation in a one-dimensional shock-tube has been solved with the initial data as given in [23] by solving the Euler equation.

The analysis and comparison of this flux vector splitting scheme with other well known methods clearly demonstrate the superior scale resolution of the proposed method, at the same time providing a neutrally stable scheme when used with four stage Runge–Kutta scheme. Also the same scheme displays extended ranges of wave numbers and circular frequencies over which DRP property is valid. The computed results of three test cases and their comparison with analytical results clearly reveal that the presented method can be used for practical problems.

Keywords: Finite volume method; Flux vector splitting schemes; Compact schemes; Nonlinear wave propagation; Shock capturing technique

* Corresponding author. Tel.: +91 512 259 7945; fax: +91 512 259 7561.
E-mail address: tksen@iitk.ac.in (T.K. Sengupta).

0021-9991/$ - see front matter © 2005 Elsevier Inc. All rights reserved.
doi:10.1016/j.jcp.2005.01.009

1. Introduction

Finite volume methods, ever since their inceptions, have been preferred by researchers for their robustness and ability to satisfy few conservation and favorable numerical properties in the physical space computations. While the early efforts using FV methods employed low order schemes, in recent times high accuracy FV method results have been reported in [6,7,17] using collocated grid and in [8] using staggered grids for cell averaged unknowns. While [6] have employed fourth order accurate FV compact schemes, [7,17] used finite volume compact schemes for large eddy simulations. While in [6] one requires a coordinate transformation before applying the discretization scheme, in [7,17] the finite volume scheme can be directly applied in the physical space. In [8], a FV has been used on staggered grids, that is essentially based on the compact scheme of Lele [2]. All these compact scheme based FV methods display wide scale resolution ability. For example, in [8] it has been shown to resolve twice the range of wave numbers as compared to the standard fourth order scheme, if one admits less than one percent filtering by the discretization of the first derivatives.

Other works that have used compact schemes within finite difference or finite volume context are given in [14–21]. In [14], Lax–Friedrich flux–vector splitting scheme was used, while Ravichandran [15] proposed a compact scheme based on kinetic flux vector splitting scheme in the finite difference context. In [21] higher order upwind compact scheme was proposed to solve hypersonic transition problems in a finite difference framework. Gaitonde and Shang [16] were perhaps the first to apply compact schemes in finite volume context for computational electro-magnetics and wave propagation problems.

The compact schemes provide high resolution and high formal order of accuracy for discretizing and filtering operators and variables and derive the name due to compact stencils that are employed. Achieving high resolution is the main goal of compact schemes and not necessarily high order – a point that has been emphasized in [4,1]. One of the attributes of the compact schemes is their usage in transformed plane and therefore one obtains schemes using uniformly distributed grid points. While compact schemes have been employed in FV methods – as discussed above – we are not aware of any efforts that have been made for flux–vector splitting FVMs. The concept of flux vector splitting is rooted to the fact that the physical fluxes crossing the boundaries of control surfaces that are constructed for the FVMs can be split depending on the sign of the eigenvalues of the associated Jacobian matrices. Mathematically this is facilitated by the fact that the fluxes are homogeneous function of order one for the unknowns. The basic ideas behind the high resolution flux vector splitting is given in [9–11]. This involves interpolating variables within each cell in terms of the cell-averaged quantities, that admits jump discontinuities. Such interpolants, valid within each cell involves first and second differences. In [10,11] these differences were estimated by lowest order centered expressions. The overall accuracy of the FVM is thus determined by the level of accuracy of such interpolations. In the present work we improve the property of the higher order interpolation by using compact differences instead to fix the parameters of the interpolant.

The paper is structured in the following manner. In the next section we derive the new scheme – which we call as the FV^2S scheme. In Section 2, properties of the FV^2S scheme are presented and compared with other existing methods. In Section 3, we present results for a few test problems using FV^2S and discuss them in the context of solving wave propagation problems and shock capturing ability of the scheme.

2. Derivation of the FV^2S scheme

In this section, we outline the steps by which we derive the new flux vector splitting finite volume method. In deriving this new scheme, we consider the solution to be piecewise continuous in each cell, as is customary for flux in high resolution flux vector splitting scheme. The schematic of unknowns within

each cell is shown in Fig. 1 for one dimensional variation. Thus, in the jth cell the unknown is continuous and is given by (see [10,11] for details),

$$u(x) = u_j + \frac{D_j u}{h}(x - x_j) + \frac{3D_j^2 u}{2h^2}\lambda\left[(x - x_j)^2 - \frac{h^2}{12}\right], \tag{1}$$

where $h = x_{j+1/2} - x_{j-1/2}$ is the cell width and u_j is the cell averaged value of the unknown defined as $u_j = \frac{1}{h}\int_{x_{j-1/2}}^{x_{j+1/2}} u(x)\mathrm{d}x$. In the above expression λ is a constant that is not fixed. Also, in Eq. (1) D_j and D_j^2 are respectively the first and second differences. Different values of λ are chosen (see [10,11] for details) to obtain different ordered schemes. For example, when the differences were chosen as, $D_j = \frac{u_{j+1} - u_{j-1}}{2}$ and $D_j^2 = u_{j-1} - 2u_j + u_{j+1}$, the following schemes were obtained: Second order central difference (CD_2) scheme for $\lambda = 1$; QUICK scheme for $\lambda = 1/2$ and a third order accurate scheme for $\lambda = 1/3$ among other schemes that can be obtained.

In the present scheme, we will use Eq. (1) as the interpolant, but we will obtain the two differences in it by obtaining them from the high accuracy scheme of [1] for the first derivative and a scheme of [2] for the second derivative. In many problems of mathematical physics the first derivative terms represent the process of convection while the second derivative terms represent diffusion process. For convection process, the information propagates directionally and hence it is natural to choose upwinded schemes that pass the signal without numerical instabilities. In contrast, the diffusion process is isotropic and the corresponding derivative is centrally discretized. These schemes for first and second differences are given in the following. For the evaluation of the first difference, the following internal stencil is used for the jth interior point,

$$b_{j-1}u'_{j-1} + b_j u'_j + b_{j+1}u'_{j+1} = \frac{1}{h}\sum_{k=-2}^{2} a_{j+k}u_{j+k}, \tag{2}$$

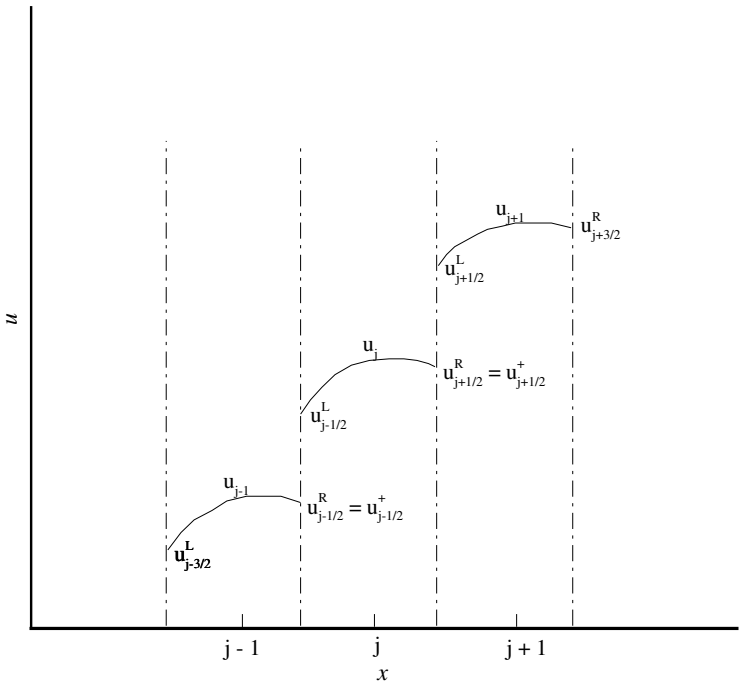

Fig. 1. Piecewise continuous representation of solution used for higher order reconstruction schemes.

with $a_{j\pm2} = \pm\frac{5}{3} + \frac{5}{6}\alpha$; $a_{j\pm1} = \pm\frac{140}{3} + \frac{20\alpha}{3}$; $a_j = -15\alpha$; $b_{j\pm1} = 20 \pm \alpha$ and $b_j = 60$ and $\alpha = -0.24$. This is essentially a fifth order upwind scheme given in [1] following the stencil given in [21]. The upwinding is needed to avoid numerical instability and achieved via negative feedback stabilization obtained through introduction of even derivatives (in this case, a sixth derivative term).

This scheme needs boundary closure at two points at and near the boundaries for non-periodic problem. The following boundary stencil have been used (as derived and explained in [10]),

$$u'_1 = \frac{(-3u_1 + 4u_2 - u_3)}{2h}. \tag{3}$$

For the near-boundary points, the following stencil is proposed

$$u'_2 = \left[\left(\frac{2\beta}{3} - \frac{1}{3}\right)u_1 - \left(\frac{8\beta}{3} + \frac{1}{2}\right)u_2 + (4\beta + 1)u_3 - \left(\frac{8\beta}{3} + \frac{1}{6}\right)u_4 + \frac{2\beta}{3}u_5\right] \Big/ h. \tag{4}$$

This composite scheme was introduced in [1] as the first optimized upwind compact scheme (OUCS1). The value of β in Eq. (4) is chosen as -0.09 for $j = 2$ and 0.12 for $j = n - 1$, where n is the total number of cells. There is a specific reason for the choice of Eqs. (3) and (4). It has been shown in [1,10] that many commonly used compact schemes for non-periodic problems suffer from numerical instability due to the choice of one-sided implicit boundary closure schemes. Such instabilities percolate in the interior of the computational domain as well. One way to avoid such numerical instabilities in the interior is to replace the implicit boundary closure scheme by explicit dissipative schemes that completely eliminates the problem. The details of upwind compact schemes can be found in [1,10].

For the evaluation of the second difference, the scheme given by Eq. (2.2.7) in [2] for second derivative has been used here. The boundary closure for the scheme is as provided in [10] and the full scheme is provided below for completeness sake,

$$u''_1 + 11u''_2 = \frac{(13u_1 - 27u_2 + 15u_3 - u_4)}{h^2}, \tag{5}$$

$$u''_1 + 10u''_2 + u''_3 = \frac{12(u_3 - 2u_2 + u_1)}{h^2}, \tag{6}$$

$$\alpha u''_{j-1} + u''_j + \alpha u''_{j+1} = \frac{b}{4h^2}(u_{j-2} - 2u_j + u_{j+2}) + \frac{a}{h^2}(u_{j-1} - 2u_j + u_{j+1}), \tag{7}$$

where $\alpha = 2/11$; $a = 12/11$ and $b = 3/11$. This is a formally sixth order scheme [2].

The above two methods for evaluating the differences can be written down notationally as,

$$[A_1]\{D_j u\} = [B_1]\{u\}, \tag{8}$$

$$[A_2]\{D_j^2 u\} = [B_2]\{u\}. \tag{9}$$

These implicit relations can be rewritten in explicit form given by

$$\{D_j u\} = [C_1]\{u\}, \tag{10}$$

$$\{D_j^2 u\} = [C_2]\{u\}. \tag{11}$$

Thus, from Eq. (1) one can obtain the cell-interface quantities for the jth-cell of Fig. 1 as

$$\{u^{\mathrm{L}}\} = [C^{\mathrm{L}}]\{u\}, \tag{12}$$

$$\{u^{\mathrm{R}}\} = [C^{\mathrm{R}}]\{u\}, \tag{13}$$

with,

$$[C^{\mathrm{R}}] = [I] + \frac{1}{2}[C_1] + \frac{\lambda}{4}[C_2], \tag{14}$$

$$[C^{\mathrm{L}}] = [I] - \frac{1}{2}[C_1] + \frac{\lambda}{4}[C_2]. \tag{15}$$

These equations would be used for calculating the cell interface variables in FV^2S, that retain the correct physical distribution of fluxes. It is to be noted that the constant, λ is a free parameter of the scheme, that can be fixed by looking at the relevant numerical properties of the FV^2S scheme. This is attempted next.

3. Spectral properties of FV^2S scheme

In analyzing the specific properties of this scheme, we consider the following one dimensional flux transport problem,

$$\frac{\partial u}{\partial t} + \frac{\partial f}{\partial x} = 0, \tag{16a}$$

where the flux term is considered to be homogeneous function of order one of the state vector. The above equation can be rewritten as

$$\frac{\partial u}{\partial t} + A\frac{\partial u}{\partial x} = 0, \tag{16b}$$

where A is the Jacobian of the flux function, f. The spectral resolution of general discretization schemes can be obtained following the method of [1] and the corresponding details are as in [10]. However, a brief outline is provided here for finite volume methods for the sake of completeness. In this method, the cell-averaged quantities are represented by

$$u_j = \int_{-k_m}^{+k_m} U(k)\mathrm{e}^{\mathrm{i}kx_j}\,\mathrm{d}k. \tag{17}$$

In the above, the integral is performed over the range $-k_m \leqslant k \leqslant +k_m$, that is fixed by the grid resolution and given by $k_m = \frac{\pi}{h}$. This is the well known Nyquist criterion that fixes the resolution of the discrete finite grid as opposed to the theoretical limit $(-\infty, +\infty)$.

The flux term (f), is split further numerically into components via $f_{\mathrm{eq}} = A^+u^+ + A^-u^-$, where $u^{\pm}$ are the state vector propagating in the downstream and upstream direction, respectively. The flux Jacobian A, is split into the respective directions using the right eigenvector (R) and eigenvalues ($\Lambda^{\pm}$) as $A^{\pm} = R\Lambda^{\pm}R^{-1}$.

In [10] the spectral resolution or the effectiveness of any flux vector splitting scheme is defined as,

$$\frac{k_{\mathrm{eq}}}{k} = \frac{f_{\mathrm{eq}}}{f} = \frac{A^+u^+ + A^-u^-}{Au}. \tag{18a}$$

The above expression on the right hand side represents the quotient between the numerical flux to the physical flux term and ideally it should be equal to one. For the flux–vector component, this represents a scalar quantity and thus, gives the phase representation of the discretized term.

Noting that $A = R(\Lambda^+ + \Lambda^-)R^{-1}$, the above can be simplified further as

$$\frac{k_{\mathrm{eq}}}{k} = \frac{\Lambda^+}{\Lambda^+ + \Lambda^-}\frac{u^+}{u} + \frac{\Lambda^-}{\Lambda^+ + \Lambda^-}\frac{u^-}{u}. \tag{18b}$$

Referring to Fig. 1, one can obtain the ratios $\frac{u^{\pm}}{u}$ using the FV^2S scheme. Another fact to note is that $\frac{k_{eq}}{k}$ does not depend on the specific value of the ratio $\frac{A^+}{A^+ + A^-}$ i.e. on the exact form of the flux function. If we call this as α then the spectral resolution of the scheme is given by

$$\frac{k_{eq}}{k} = \alpha \frac{u^+}{u} + (1-\alpha)\frac{u^-}{u}. \tag{18c}$$

If we decide to evaluate this at the left boundary of the jth-cell, then in Eq. (18c) we calculate the unknowns from Eqs. (11) and (12) by noting that $u^+_{j-1/2}$ is u^R of the $(j-1)$th-cell and $u^-_{j-1/2}$ is u^L of the jth-cell. The presented method for characterizing the numerical scheme, by adopting the method of [1], allows one to investigate the full domain simultaneously. It is to be noted that the usual practice followed so far in the literature, has been to characterize schemes simply based on the performance of the schemes for interior points only. For the present exercise, we have used 51 point for the purpose of analysis, ensuring that the presented results do not depend on the choice of number of points.

In Fig. 2(a), the real part of $\frac{k_{eq}}{k}$ is compared with other known finite volume schemes for the interior nodes only. For FV^2S scheme, results are shown for $\lambda = 0.4$ and 0.6. For the purpose of comparison we have included the second order central difference scheme in Fig. 2, denoted by CD_2 scheme. We have already remarked that λ is a constant that needs to be fixed based on numerical properties. It is evident that for $\lambda = 0.6$ we have reduced over- and undershoot for $\frac{k_{eq}}{k}_{real}$ as compared to that for $\lambda = 0.4$. However, it is shown later that the wave propagation property of the scheme – as given by the DRP property – requires that one chooses $\lambda = 0.4$. The results in Fig. 2(a) show that the present scheme has almost twice the range of wave numbers well resolved as compared to other well known schemes like $QUICK$ or $MUSCL$. The results for these latter flux vector splitting schemes were reported in [12,10]. The present FV^2S scheme also has marginally larger resolution as compared to the finite volume method of [8] – that is marked as $OCS4$ in the figure. It is noted that $MUSCL$ and $OCS4$ schemes have slight overshoot across low wave numbers, while FV^2S has undershoot for $\lambda = 0.6$ and overshoot for $\lambda = 0.4$ at lower wave numbers. This figure only provides the phase information of different FV schemes for the interior stencils. Also, in Fig. 2(b) the imaginary part of $\frac{k_{eq}}{k}$ is shown for these flux vector splitting FV schemes. It can seen that all the schemes show positive values – indicating added numerical dissipation at different length scales, being more at larger wave numbers – a desirable feature of any numerical schemes. Note that the CD_2 scheme is a central scheme and is non-dissipative.

In Fig. 3, the real and imaginary part of $\frac{k_{eq}}{k}$ is shown for FV^2S scheme for $\lambda = 0.4$ and 0.6 for some representative points in the full domain using Eqs. (3) and (4) as the boundary closure schemes. In plotting these figures a fourth dissipation term has been added to stabilize the finite volume spatial discretization process. For the jth cell, the added numerical dissipation is given by, $D_j = \frac{d_{j+1/2} - d_{j-1/2}}{h}$, where the dissipation term on the cell face is given by $-\beta_2(u_{j+2} - 3u_{j+1} + 3u_j - u_{j-1})$. It is clear that the scheme performs well for all the points except for $j = 2$, even after adding the numerical dissipation term. This point is unstable, while all the other points are made stable by introduction of the dissipation term. In an actual application, at $j = 2$, a CD_2 type non-dissipative scheme is to be employed to avoid numerical instability. Such substitution by an explicit scheme does not alter any other point properties and can be used for any computation. This type of treatment has been used by the authors in finite difference context in [1,10] for solving inviscid and viscous flow problems. For convection dominated flows, numerical instability will not cause problems if the disturbances are convected downstream from the inflow to the interior of the domain, where it will find itself in stable region with time. Furthermore, such tendencies of spatial discretization can further accentuate or attenuate depending on time integration strategies. This implies that one should obtain the amplification factor of the combined space–time integration strategy.

The stability property of the combined space–time discretization scheme can be ascertained with respect to specific equation and to study propagation problems, we use one-dimensional convection equation for this purpose:

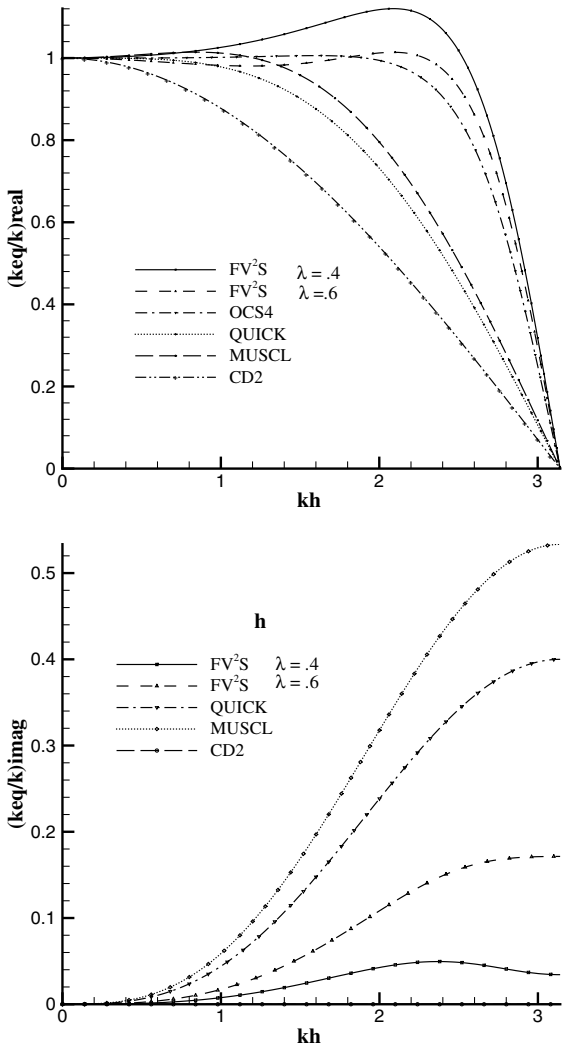

Fig. 2. Spectral resolution of some high accuracy finite volume schemes. Second order central scheme (CD2) is included for comparison. QUICK and MUSCL schemes are from [12] and OCS4 is from [8].

$$\frac{\partial u}{\partial t} + c\frac{\partial u}{\partial x} = 0. \tag{19}$$

If we use the bi-lateral Laplace transform for u given by

$$u(x,t) = \int U(k,t)\mathrm{e}^{\mathrm{i}k(x-ct)}\mathrm{d}k, \tag{20}$$

then we define the amplification factor of the numerical scheme by $G = U(k,t+\Delta t)/U(k,t)$. For the above equation, information propagates from left to right that leads to the following flux vector splitting given by

$$\frac{u_j^{n+1} - u_j^n}{\Delta t} + c[u^+_{j+1/2} - u^+_{j-1/2}]h = 0, \tag{21}$$

when Euler time integration strategy is used to advance the time step from t^n to t^{n+1}. Using $N_c = \frac{c\Delta t}{h}$ for the CFL number and Eqs. (12) and (13), the amplification factor at the jth-cell is obtained as,

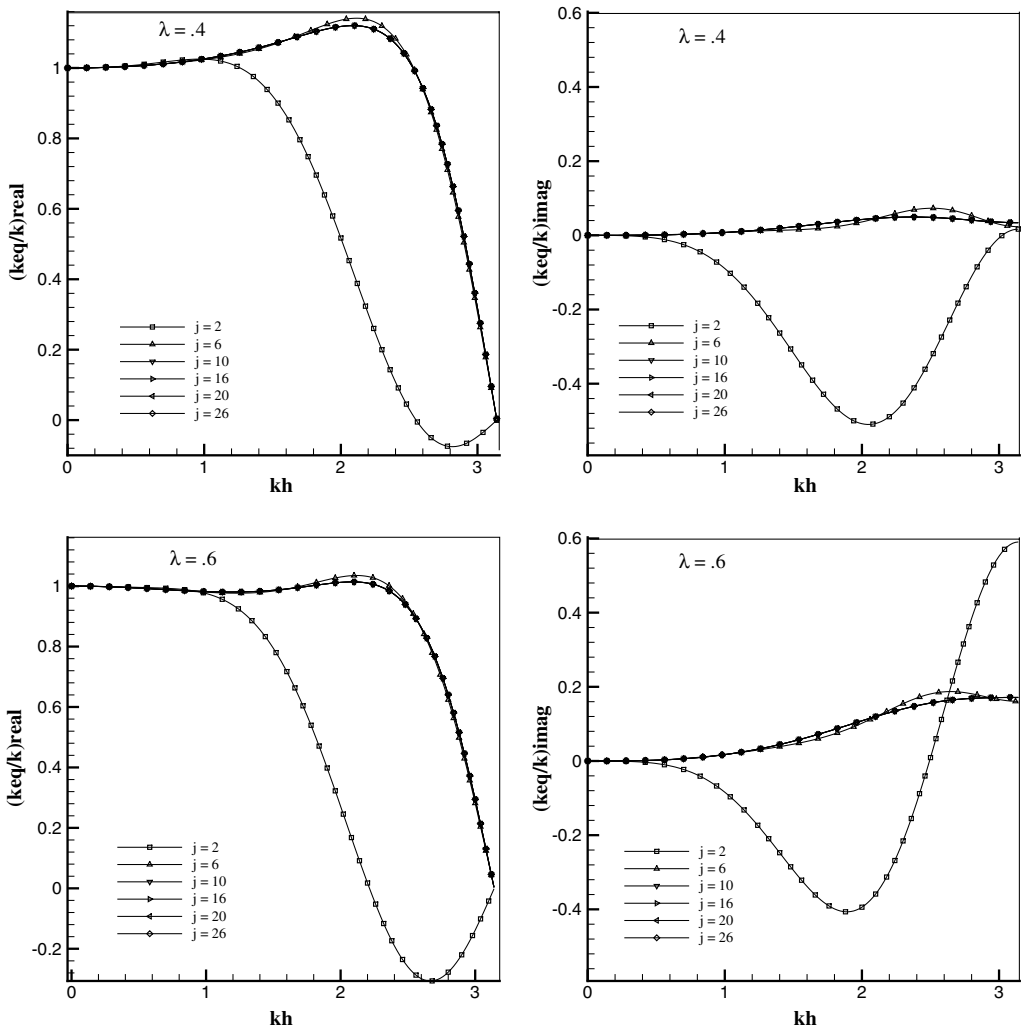

Fig. 3. Spectral resolution of FV2S – scheme for representative points in the full domain for two values of λ (as introduced in Eq. (1)).

$$G_j(k) = 1 - N_c \sum_{l=1}^{N} [C^R_{j,l} - C^R_{j-1,l}] e^{ik(x_l - x_j)}. \tag{22}$$

We have also used four-stage Runge–Kutta time integration scheme (RK4) to be used with FV^2S-scheme. If we denote by $L(u) = -c\frac{\partial u}{\partial x}$, then the steps used in RK4 are given by

$$\begin{aligned}
&\text{Step 1}: \quad u^{(1)} = u^{(n)} + \frac{\Delta t}{2} L[u^{(n)}],\\
&\text{Step 2}: \quad u^{(2)} = u^{(n)} + \frac{\Delta t}{2} L[u^{(1)}],\\
&\text{Step 3}: \quad u^{(3)} = u^{(n)} + \Delta t L[u^{(2)}],\\
&\text{Step 4}: \quad u^{(n+1)} = u^{(n)} + \frac{\Delta t}{6}\{L[u^{(n)}] + 2L[u^{(1)}] + 2L[u^{(2)}] + L[u^{(3)}]\}.
\end{aligned} \tag{23}$$

If we define,

$$A_j = N_c \sum_{l=1}^{N} [C^R_{j,l} - C^R_{j-1,l}] e^{ik(x_l - x_j)}, \tag{24}$$

then it is easy to show that the amplification factor at the jth-cell for the RK4 time integration scheme is,

$$G_j(k) = 1 - A_j + \frac{A_j^2}{2} - \frac{A_j^3}{6} + \frac{A_j^4}{24}. \tag{25}$$

The amplification factors are shown in Fig. 4 for $N_c = 0.01$ and 1 for the FV^2S scheme when used with Euler and RK4 time integration scheme. It is evident that the Euler time integration scheme is stable for all cells except for $j = 2$. However, this scheme shows large attenuation at large wave numbers for other cells – that is not suitable for high accuracy computing. In contrast, RK4 scheme provides near neutral stability for all cells for all wave numbers. Thus, RK4 time integration is preferred from numerical stability point of view.

The dispersion relation preservation is a mandatory property for schemes used to produce results valid for long time intervals over large domains for propagation problems. This property must not be violated for any scheme to be considered for DNS and acoustics or any other nonlinear wave propagation problems. The dispersion relation is a property specific to physical systems as defined by the governing differential equation and for the convection equation this is given by, $\omega = kc$. Any numerical scheme must satisfy the physical dispersion relation for unsteady problems in general. As the energy of convective dispersive system travels at the group velocity, the dispersion relation preservation (DRP) property is assessed by comparing numerical and physical group velocity [10]. One can obtain the numerical group velocity from the numerical dispersion relation (see [13] for full details as to how this can be evaluated). For the convection equation this is given by, $\omega_{eq} = kc_N$, where the numerical phase speed is, $c_N = \frac{\beta_1}{k\Delta t}$. The phase angle is obtained from the amplification rate as, $\tan(\beta_1) = -\frac{G_{imag}}{G_{real}}$. Since the group velocity is defined as $V_{gN} = \frac{d\omega_{eq}}{dk}$, the ratio of numerical and physical group velocity for the convection equation can be shown as

$$\frac{V_{gN}}{c} = \frac{1}{N_c h} \frac{d\beta_1}{dk}. \tag{26}$$

For the FV^2S scheme when used with Euler time integration strategy the DRP property is simply assessed by evaluating the numerical group velocity from Eq. (26) directly, when β_1 as a function of k is directly obtained from Eq. (22). For RK4 time integration scheme, the phase angle β_1 is obtained from Eq. (25) and differentiated with respect to k by using Eq. (21).

The numerical group velocity is compared with the physical group velocity in the $(kh - \omega\Delta t)$ – plane as shown in Figs. 5 and 6 for Euler and RK4 time integration strategy, respectively. To compare the relative merits of the two time integration schemes, these figures are drawn for the basic spatial discretization without the explicit dissipation terms. Contour lines of the ratio of Eq. (26) are plotted only in the range $0.95 \leqslant \frac{V_{gN}}{c} \leqslant 1.05$. From Fig. 5, it is seen that the Euler time integration restricts one to very small time steps in order to satisfy DRP criterion. In the six frames of Fig. 5, different values of λ have been considered. It is seen that the increase of this parameter restricts the range of wave numbers that satisfy the DRP property criterion, with a value of $\lambda = 0.4$ proving to be optimum when the DRP property and the spectral resolution are considered together. Although the DRP patch for $\lambda = 0.33$ is larger as compared to $\lambda = 0.4$ case, $\frac{k_{eq}}{k}$ for $\lambda = 0.33$ is inferior to $\lambda = 0.4$ case. It was for this reason, in Fig. 2 we have shown this value along with $\lambda = 0.6$ – that shows relatively poor DRP property. In comparison to Euler time integration scheme, same property in Fig. 6 shows that the range of $\omega\Delta t$ over which DRP property is good extends by order of magnitude – covering almost 50% of the Nyquist limit. It is also noted that λ in the range of 0.3–0.4 shows the largest range of kh allowed from DRP property point of view. For $RK4$ scheme,

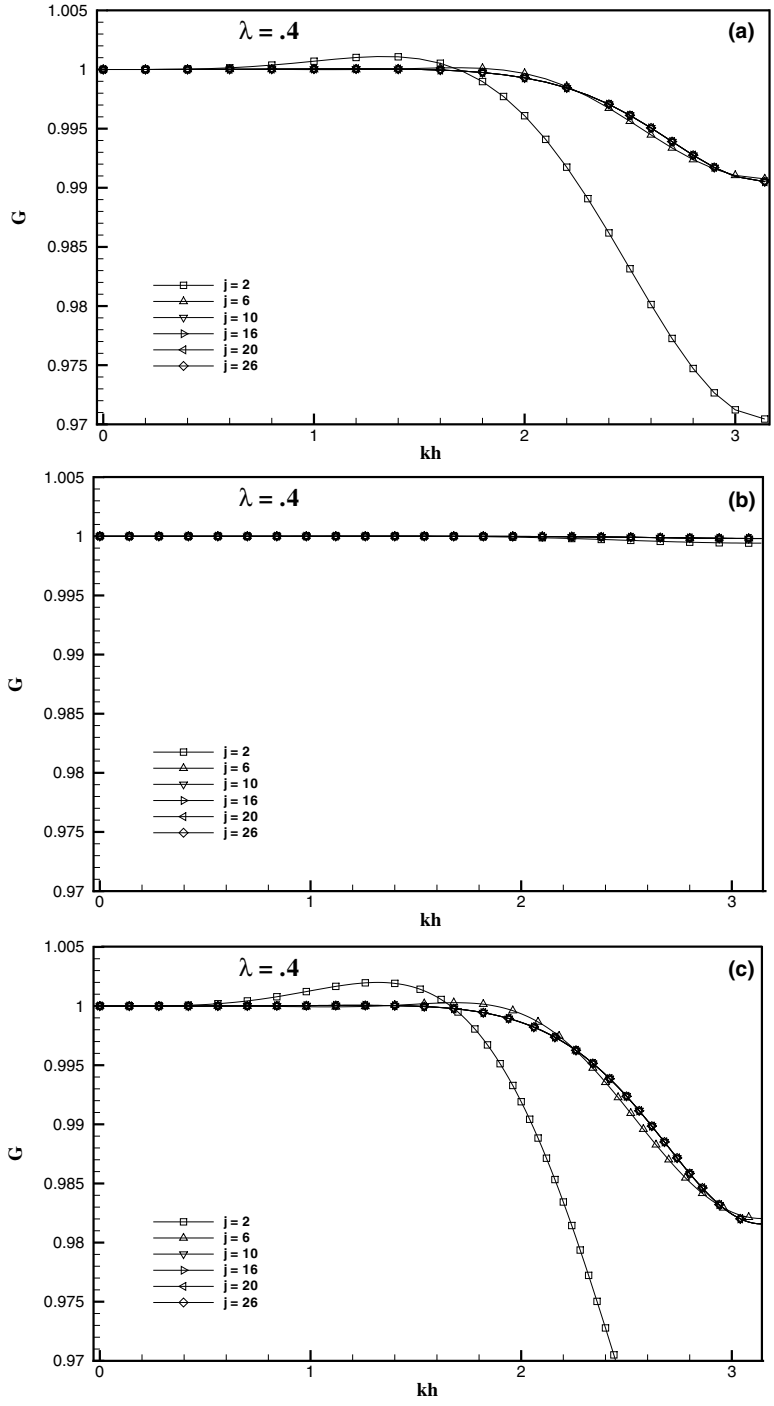

Fig. 4. The amplification factor for convection equation (Eq. (20)) discretized by FV^2S – scheme along with (a) Euler time integration ($N_c = 0.01$); (b) and (c) RK4 time integration schemes with $N_c = 0.01$ and 1 respectively.

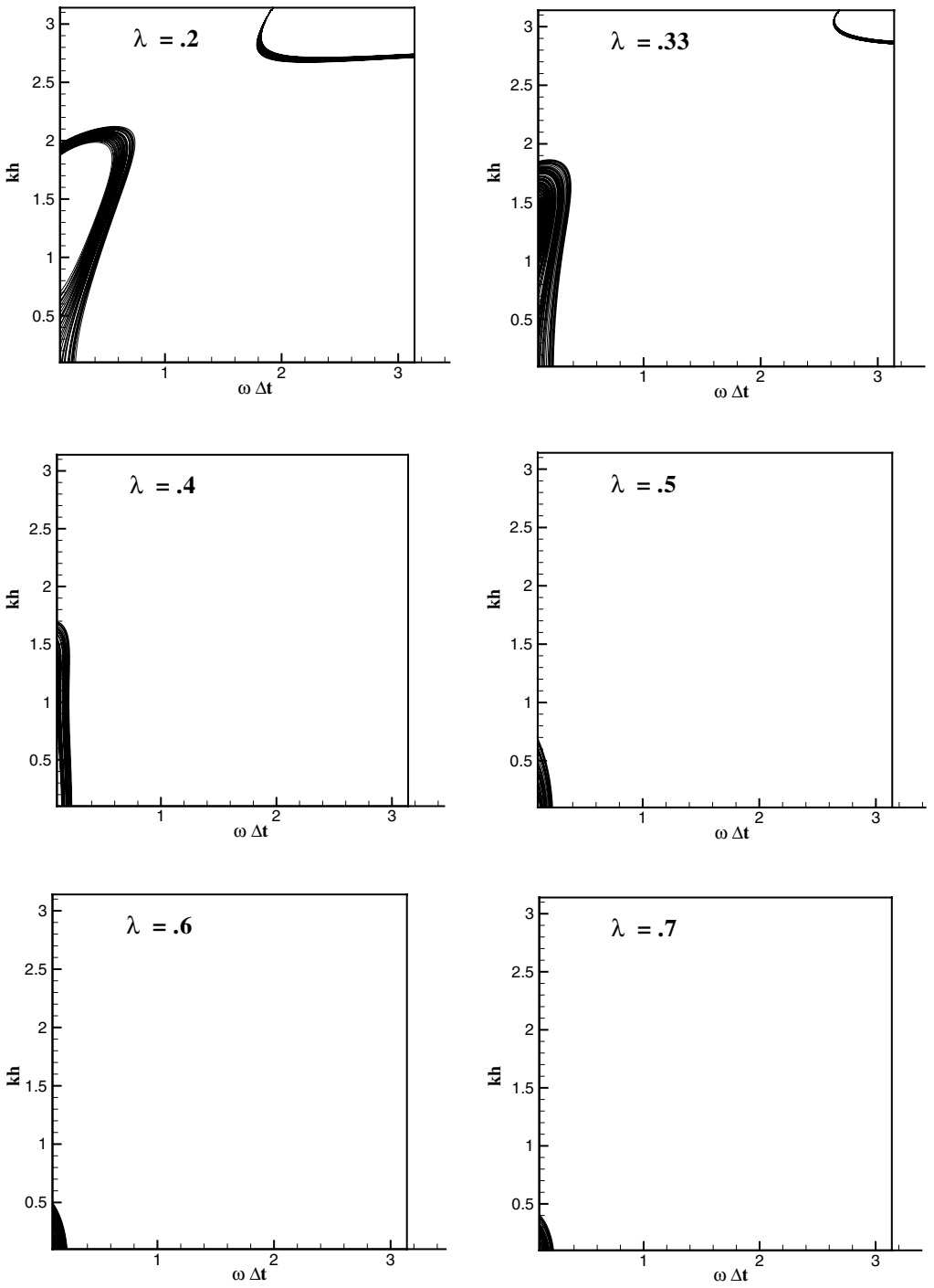

Fig. 5. Contours of (V_{gN}/c) in ($kh - \omega\Delta t$)-plane for the indicated λ's for 1D wave equation. Temporal discretization is by Euler scheme. The marked regions correspond to the contours for which $0.95 < V_{gN}/c < 1.05$.

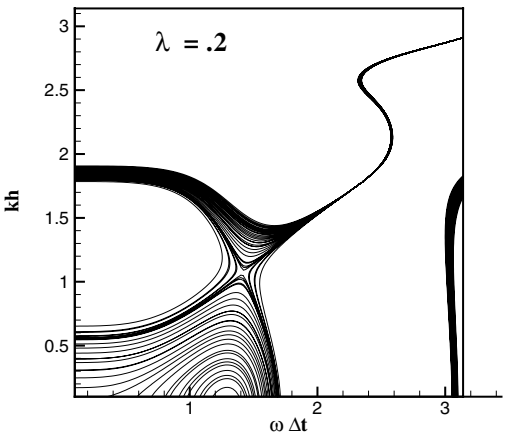

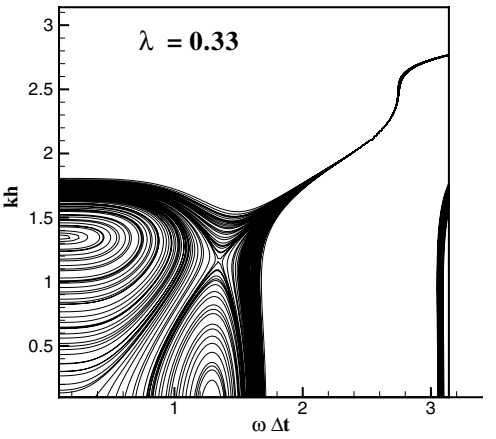

kh

kh

kh

kh

$\lambda = 0.6$ shows inferior DRP property. Thus, it is seen that spectral resolution and DRP property imposes opposite demand on the value of λ, and $\lambda = 0.4$ appears to be an optimum choice.

4. Results and discussion

In order to test the capability of the present method to capture discontinuity, linear convection equation, $\frac{\partial u}{\partial t} + c\frac{\partial u}{\partial x} = 0$, is solved with the discontinuous initial condition

$$\begin{aligned} u(x+0.5,0) &= -x\sin(3/2\pi x^2) \quad -1 < x < -1/3, \\ &= |\sin(2\pi x)| \quad |x| < 1/3, \\ &= 2x - 1 - \sin(3\pi x)/6 \quad 1/3 < x < 1. \end{aligned}$$

and supplemented with periodic boundary conditions. This test case was originally proposed by Harten et al. [3], and then used by many authors to check the capability of numerical schemes to obtain solutions with discontinuities. The solutions are reported at $t = 2$, that corresponds to a distance of one wavelength by which the initial solution travels to the right. To capture the discontinuities efficiently the dissipation switch developed in [5] is used. In this method, the second derivative of the variable ($|D_j^2|$) is used as the switch. Only at those points, where its value exceeds a threshold (equal to 30), the fourth dissipation is applied explicitly, as defined already. In principle, the numerical stabilization is similar to the procedure originally proposed in [22], where a pressure based switch was used to introduce the second derivative term at discontinuities for Euler equation of gas dynamics, while fourth derivative term was added as the background dissipation everywhere. In contrast, we do not add second dissipation term at all and the fourth dissipation term is introduced selectively at those points where the second-derivative-based switch crossed the threshold value.

Fig. 7(a) and (b) shows the solution using FV^2S scheme with Euler and RK4 time integration for $N_c = 0.001$ and $N_c = 1.0$, respectively. The solid line in the figures represent the exact solution. The rationale for the choice of N_c is very much evident from the spectral properties shown in Figs. 4–6. From Fig. 7, one can clearly see that the combination of FV^2S with RK4 time integration scheme produces accurate solution in the smooth regions and captures the discontinuities without observable oscillations. The numerical stability of the computed solution depends on the choice of N_c. With RK4 and FV^2S any choice of $N_c > 1$ caused the solution to blow up for $\beta_2 \geqslant 0.04$. Any value of $N_c \leqslant 1$ is found to be stable for $\beta_2 = 0.04$ that provided the best accuracy for this problem.

Next, we investigate sources of Gibbs' phenomenon for a non-periodic problem by solving the linear convection equation with a different set of initial condition that has been used in [10]. Here, the wave equation is solved in a domain $0 \leqslant x \leqslant 1$ for $c = 0.05$ with 201 uniformly distributed points. Convection of a wave packet, defined by the initial condition displayed in the top panel of Fig. 8 is considered in this case. For the wave equation, the initial solution convects to the right at phase speed given by c. The wave packet is chosen in such a way that the solution is zero outside the domain $0 \leqslant x \leqslant 1$ at $t = 0$. Thus, the packet has discontinuity at both the left and right end of the domain for the initial solution. With time, the packet convects to the right and only a discontinuity is present inside the computing domain up to $t = 20$. For the solution of the problem, we have used the exact boundary condition at $x = 0$ for all times. This equation is integrated first by Euler time stepping, using $N_c = 0.001$ and then by RK4 scheme with $N_c = 0.1$. Euler time marching scheme requires a very low value of N_c number to ensure numerical stability across all the resolved wave numbers determined by the Nyquist criterion.

Gibbs' phenomenon arises whenever a sharp discontinuity is computed by numerical methods and is visible as left- and/or right-running waves created by odd-order derivatives of the truncation error terms.

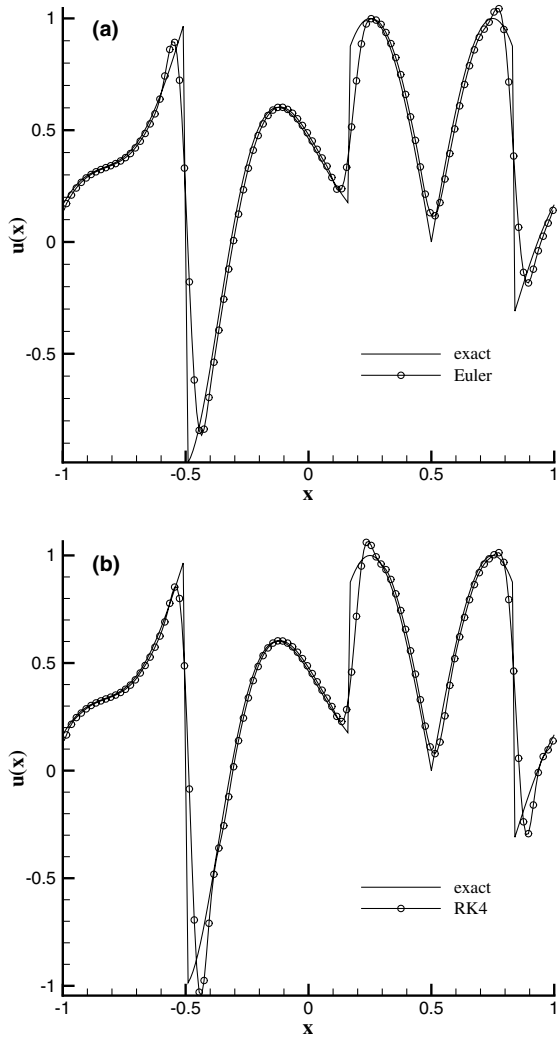

Fig. 7. Numerical solution of Eq. (20) for the test case of [3] by FV_2S – scheme along with (a) Euler ($N_c = 0.001$) and (b) RK4 ($N_c = 1$), time integration scheme.

When left uncontrolled these waves grow leading to numerical instability. From the figures it is evident that the present FV^2S scheme is capable to capture solution discontinuity for linear problems.

Next, the present scheme's ability to capture shock for a non-linear equation is studied by solving the Burgers' equation given by

$$\frac{\partial u}{\partial t} + u\frac{\partial u}{\partial x} = 0 \quad -1 \leqslant x \leqslant 1, \tag{27}$$

with the following initial condition

$$u(x,0) = 0.3 + 0.7\sin\pi(x+1) \tag{28}$$

and periodic boundary condition. This problem admits analytical solution derivable from the solution of the transcendental equation [4],

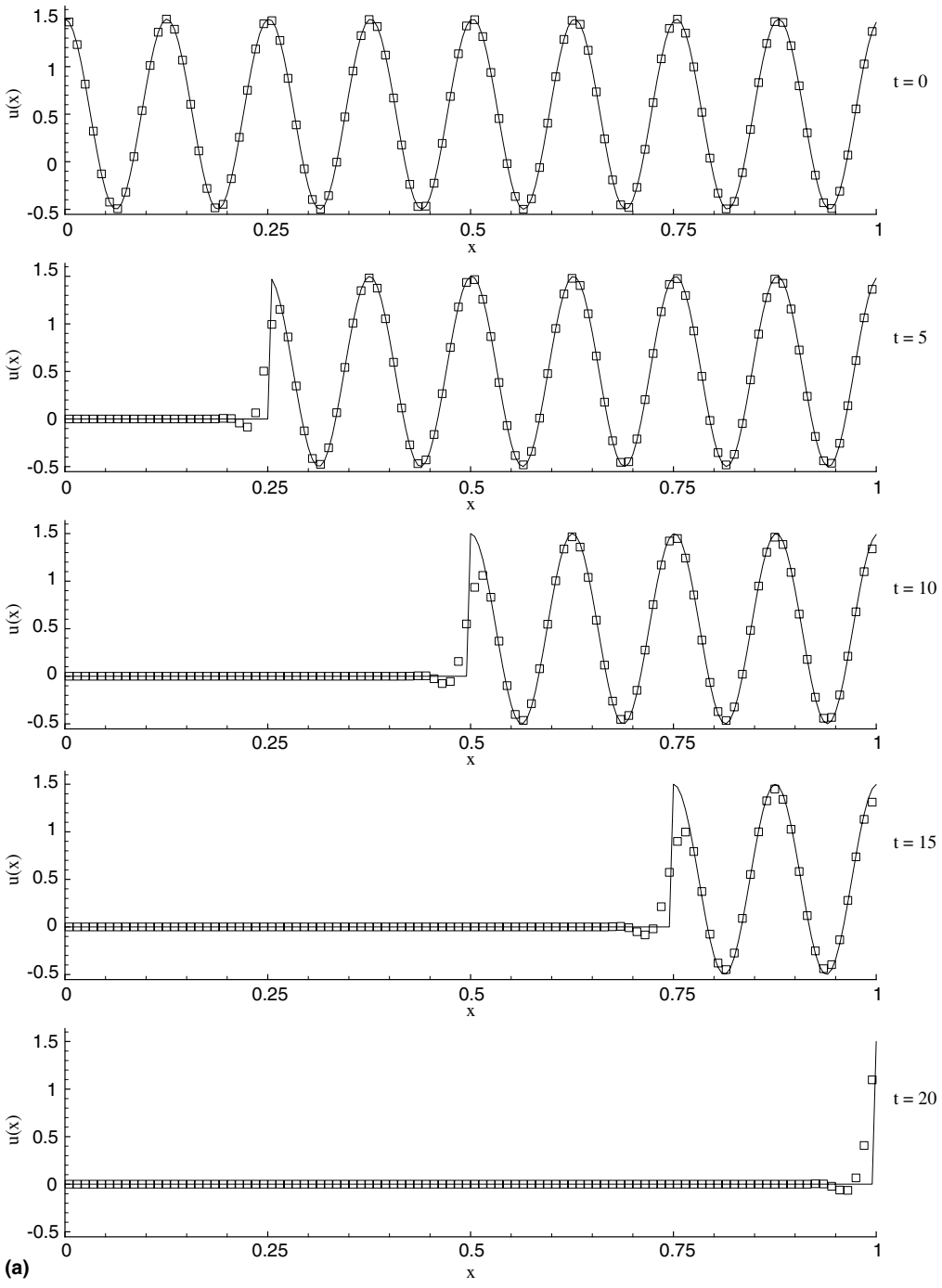

Fig. 8. Solution of convection equation at the indicated times. The computed solutions (discrete symbols) are obtained using FV^2S with (a) Euler scheme and compared with exact (solid line) solution for $c = 0.05$, $N = 201$ and $\Delta t = 0.0001$, (b) RK4 scheme and compared with exact (solid line) solution for $c = 0.05$, $N = 201$ and $\Delta t = 0.01$.

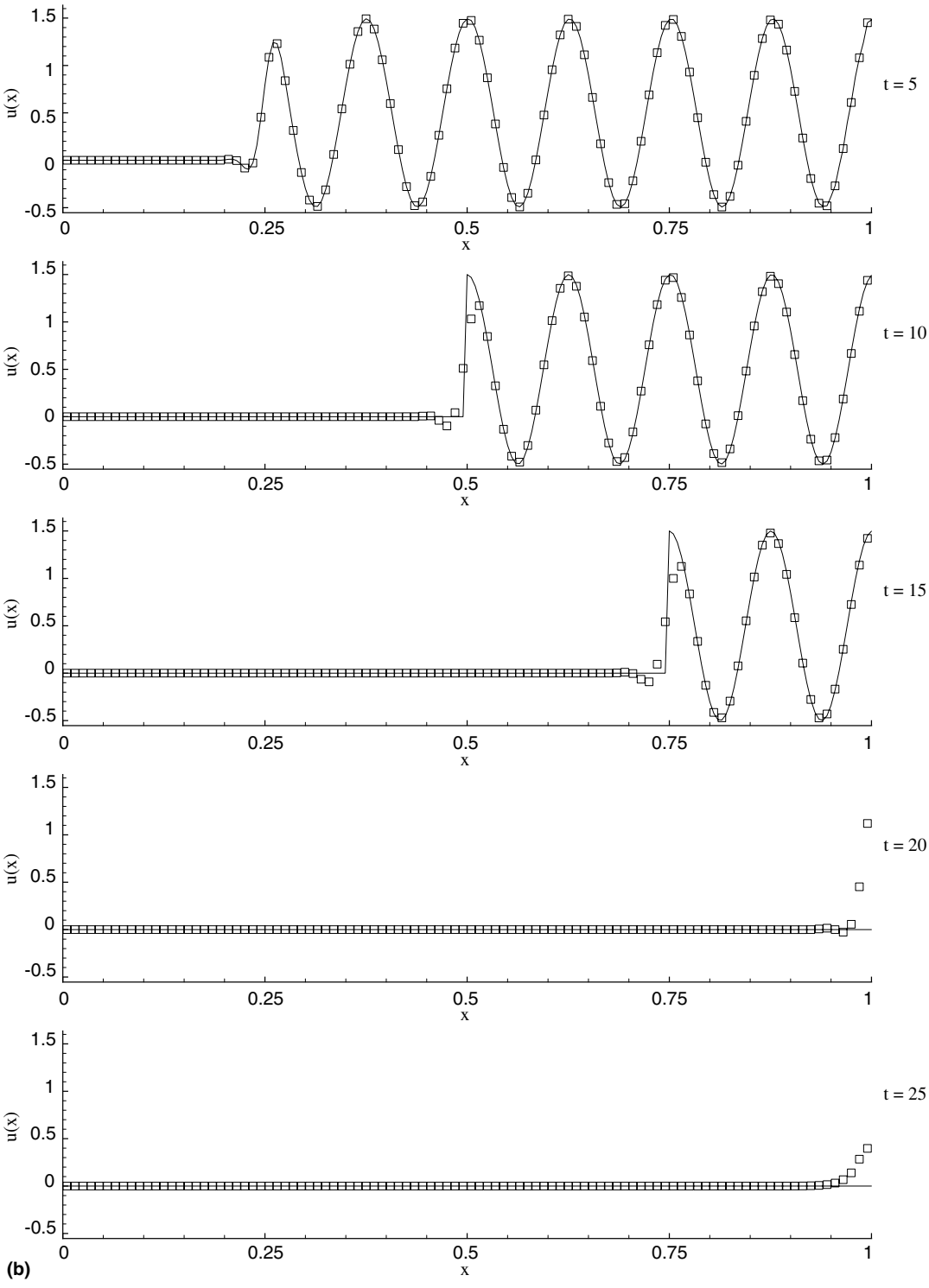

Fig. 8 (*continued*)

$$Z(\tau, \xi) = \sin[(\xi - Z(\tau, \xi)\tau)\pi]. \tag{29}$$

The solution of Eq. (27) is then obtained as $u(x,t) = 0.3–0.7\ Z(\tau,\xi)$, where $\xi = x - 0.3t + 1$ and $\tau = 0.7t$. The solution of the problem consists of a steepening wave propagating to the right, which gives rise to a shock wave at $t = 0.455$. A uniformly spaced c60-25[(=)-255.9(0.455.)-/F918.46 spaced

solution. The figure gives evidence of the capability of the newly developed FV^2S scheme to correctly compute the discontinuous solution without any oscillations. The computed solutions for the wave packet and the Burgers' equation are same for both the time integration schemes up to third decimal place.

It is to be noted that in capturing discontinuities for linear equation or shocks in non-linear equation, the present method required the same procedure that was performed in [5] for the compact finite difference method in an uniform grid. For the results of Fig. 9 and in [5], fourth dissipation term is used for negative feedback stabilization at only those points, where the amplitude of second spatial derivative exceeded a fixed high value. This type of explicit treatment to avoid Gibbs' phenomenon is simpler than the nonlinear shock capturing methods referred to in [5]. In the context of flux vector splitting schemes, one finds the mention of using *flux limiter* schemes that utilize non-linear functions for flux evaluation at control surfaces to prevent unwarranted oscillations. Apart from the complicated unexplained nature of these flux limiter schemes, these also introduce source terms in the discrete equation invalidating the continuous nature of the fluxes across such solution discontinuities. The present method obviates this problem when the excited wave numbers are limited in nature and one uses uniform grid.

One of the main advantages of finite volume method is its ability to work with irregular grids without resorting to any coordinate transformation, as is the case with finite difference methods. But for the FV^2S scheme, one would require to work on the transformed plane because its inherent dependence on compact based finite difference methods. To investigate working with non-uniform grids, we solved the Burgers' equation again using a clustered grid near the center along with the four-stage Runge–Kutta time integration scheme. Even though we are working in the transformed plane, the appearance of grid metric term will give rise to aliasing error which is not present if one works in the physical plane directly. We have used 171 grid points with 121 points clustered between $x = -0.5$ and $+0.5$ and the rest of the points are distributed uniformly over the rest of the domain. The solution is now obtained in the transformed plane (ξ) by first obtaining $x_\xi = \frac{dx}{d\xi}$ at each node and solving the transformed equation,

$$\frac{\partial u}{\partial t} + \frac{u}{x_\xi}\frac{\partial u}{\partial \xi} = 0. \tag{30}$$

The evolving shock is captured by using the blend of second and fourth dissipation as in [22] with $\kappa^{(2)} = 0.8$ and $\kappa^{(4)} = 1/32$. When only fourth dissipation is used – as in [5] – then one observes significant

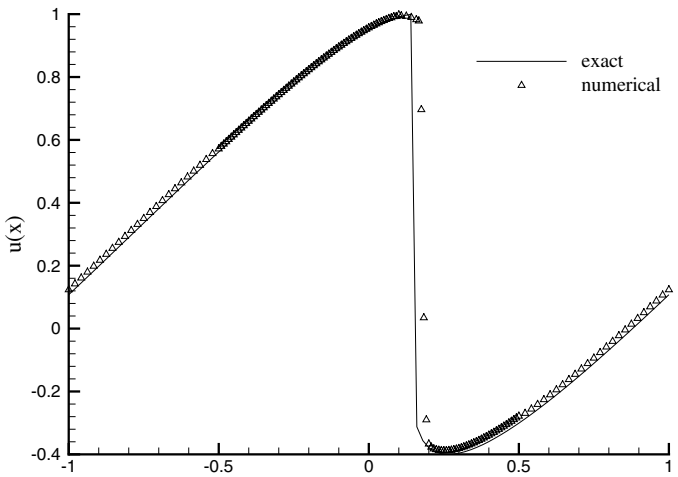

Fig. 10. Numerical solution of the Burger's equation (Eq. (25)) at $t = 0.637$ by FV^2S-scheme using a non-uniform grid. All the computational parameters are same as in Fig. 9.

Gibbs' phenomenon to the left of the shock and is not shown here. The numerically obtained solution using non-uniform grid is compared with the exact solution for $t = 0.637$ in Fig. 10. This shows that the present method is capable to produce accurate solution when used in an irregular grid. The position of the shock depends on the DRP property as has been discussed next with respect to the solution of Euler equation.

To investigate the present method's ability to solve practical problem we have solved Euler equation for the one-dimensional shock tube problem or the Riemann problem [23] using the following initial conditions ($t = 0$): $u = 0$; $p = 4.4$ for $x < -2$; $p = 2.7 + 1.7\cos\left[\frac{(x+2)\pi}{4}\right]$ for $-2 \leqslant x \leqslant 2$ and $p = 1$ for $x > 2$. With the perfect gas assumption and $\gamma = 1.4$, the governing Euler equation is solved in a computational domain, $-100 \leqslant x \leqslant 100$. This problem tests the nonlinear wave propagation property of the computational scheme

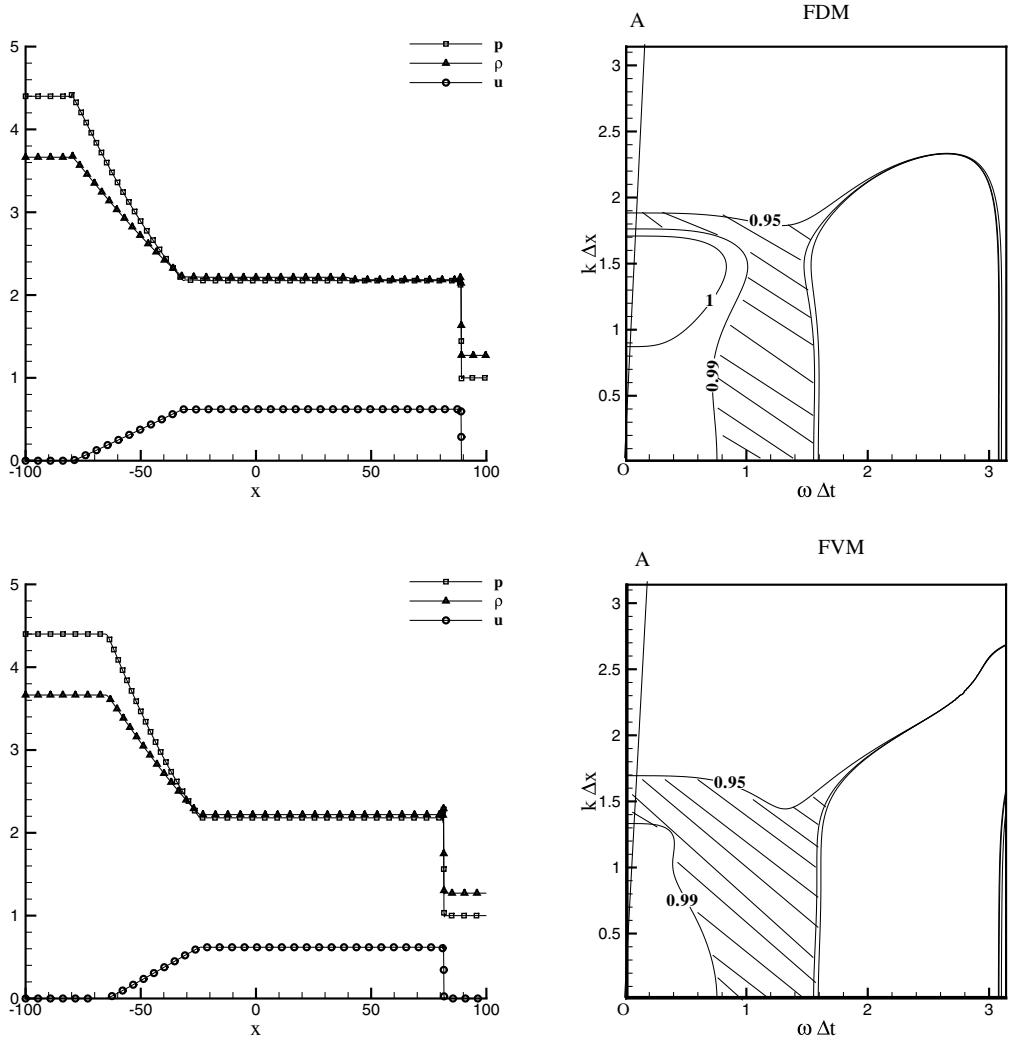

Fig. 11. The pressure, density and velocity profiles in the physical domain computed at $t = 60$ by finite difference method (top) and FV^2S finite volume method (bottom). For both the methods same compact scheme has been used for evaluating the first derivative. Right panels show the corresponding DRP plots for the basic spatial discretization scheme.

and was proposed as one of the benchmark problems for computational aero-acoustics in [23]. This problem apart from requiring numerical accuracy, also tests the dispersion relation preservation property of chosen scheme.

The given initial condition evolves into a left running acoustic wave, a convecting entropy wave and a right traveling shock wave. To check the efficacy of the present flux vector scheme's ability to capture the discontinuous solution, this solution is compared to the solution of the same problem using the compact scheme based finite difference method (FDM). For both the methods the flux vector splitting is used along with simple extrapolation boundary conditions. The used compact scheme, OUCS1, was proposed in [1] for FDM and is the same one used to develop the FV^2S scheme. The computed results at $t = 60$ are shown in Fig. 11, using these two methods. Once again, the blend of second and fourth dissipation is added – as in [22] – to capture the shock. Both the methods show the ability to capture all the traveling waves. As compared to the results reported in [23], here the contact discontinuity is captured by the FDM and not by the FV^2S method. The FV^2S method also shows Gibbs' phenomenon at the shock, while the FDM does not have this effect. The shock location and the location of the acoustic waves are somewhat different for these two methods. To understand the reason behind this, the DRP plot of the two methods are shown alongside the solutions. In these plots the normalized group velocity contours are plotted for the traveling wave equation, with the normalized contours between 0.95 and one are shown in the $(k\Delta x - \omega\Delta t)$-plane. The slope of the lines OA in these plots indicate the CFL number that has been used in the computations. Also, the region in these plane is marked by hatched lines where the waves would travel slower by 1 to 5% for a travelling wave. For the FVM, the group velocity is always less than one, while for the FDM there is a range of $k\Delta x$ between 0.88 and 1.7, for which the numerical group velocity is higher than the physical group velocity and hence the computed shock will move faster than what it should be. Also, the range of $k\Delta x$ for which the numerical wave components travel slower is narrower for FDM as compared to FV^2S scheme. The overall results of which show that the left running acoustic wave and the right traveling shock wave both move farther than the corresponding waves calculated by FV^2S.

Finally, some comments are in order for using the proposed scheme here for multidimensional problems. Using structured grids, this did not cause any problem by treating each directions separately while discretizing the differential equations by FDM based on compact schemes. A large number of such cases have been solved and reported by the present authors that have been reported in [10] and references therein. For FV^2S scheme this has to be attempted. When the present flux vector splitting FVM is compared with the corresponding FDM, then it is found that the FVM requires more computational work without any additional accuracy of the method. The presented results here are preliminary in nature and we plan to investigate the scheme further to improve the efficacy and efficiency of this method.

5. Conclusions

A new flux–vector splitting compact finite volume Scheme (FV^2S) has been developed here. This scheme has been analyzed by the matrix-spectral analysis tool developed in Sengupta et al. [1]. It is shown that FV^2S has high spectral accuracy and has the capability to capture discontinuity for linear problems that could be periodic or non-periodic. The periodic problem is the well known test problem of Harten et al. [3] and the non-periodic problem is the propagation of a wave-packet that was computed in [1,5,10].

Capturing shocks for non-linear problem is addressed here by solving the Burgers' equation and the Riemann problem. The computed solutions match very well with the analytical solution given in [4,23]. As proposed in [5], the numerical methods have been stabilized by introducing fourth dissipation term at only those points where the second derivative exceeded a prefixed high value.

References

[1] T.K. Sengupta, G. Ganeriwal, S. De, J. Comput. Phys. 192 (2003) 677.
[2] S.K. Lele, J. Comput. Phys. 103 (1992) 16.
[3] A. Harten, B. Engquist, S. Osher, S. Chkravarthy, J. Comput. Phys. 71 (1987) 213.
[4] N.A. Adams, K. Shariff, J. Comput. Phys. 127 (1) (1996) 27.
[5] T.K. Sengupta, G. Ganeriwal, A. Dipankar, J. Sci. Comput. 21 (3) (2004) 253.
[6] J.M.C. Pereira, M.H. Kobayashi, J.C.F. Pereira, J. Comput. Phys. 167 (2003) 217.
[7] S. Smirnov, C. Lacor, M. Baelmans, AIAA paper 15th AIAA Computational Fluid Dynamics Conference, June 11–14, Anaheim, CA, 2001.
[8] M. Piller, E. Stalio, J. Comput. Phys. 197 (2004) 299.
[9] B. Van Leer, J. Comput. Phys. 32 (1979) 101.
[10] T.K. Sengupta, Fundamentals of Computational Fluid Dynamics, University Press, Hyderabad, India, 2004.
[11] C. Hirsch, Numerical Computation of Internal and External Flows, Wiley, New York, 1998.
[12] T.K. Sengupta, S. Sridar, S. Sarkar, S. De, Int. J. Numer. Meth. Fluids 35 (2001) 149.
[13] T.K. Sengupta, A. Dipankar, J. Sci. Comput. 21 (2) (2004) 225.
[14] B. Cockburn, C.W. Shu, SIAM J. Numer. Anal. 31 (3) (1994) 607.
[15] K.S. Ravichandran, J. Comput. Phys. 130 (1997) 161.
[16] D.S. Gaitonde, J.S. Shang, J. Comput. Phys. 138 (1997) 617.
[17] C. Lacor, S. Smirnov, M. Baelmans, J. Comput. Phys. 198 (2004) 535.
[18] J.A. Ekateranaris, J. Comput. Phys. 156 (1999) 272.
[19] J.A. Ekateranaris, AIAA J. 38 (9) (2000) 1594.
[20] H. Dong, X. Zhong, AIAA J. 40 (5) (2002) 869.
[21] X. Zhong, J. Comput. Phys. 144 (1998) 622.
[22] A. Jameson, W. Schmidt, E. Turkel, AIAA paper no. AIAA-81-1259. Presented at AIAA 14th Fluid and Plasma Conf. (1981).
[23] J.C. Hardin, J.R. Ristorcelli, C.K.W. Tam, ICASE/ LaRC Workshop on benchmark problems in computational aeroacoustics. NASA Conf. Publ. 3300 (1995).